iScience

CellPress
OPEN ACCESS

Article

ATP mimetics targeting prolyl-tRNA synthetases as a new avenue for antimalarial drug development

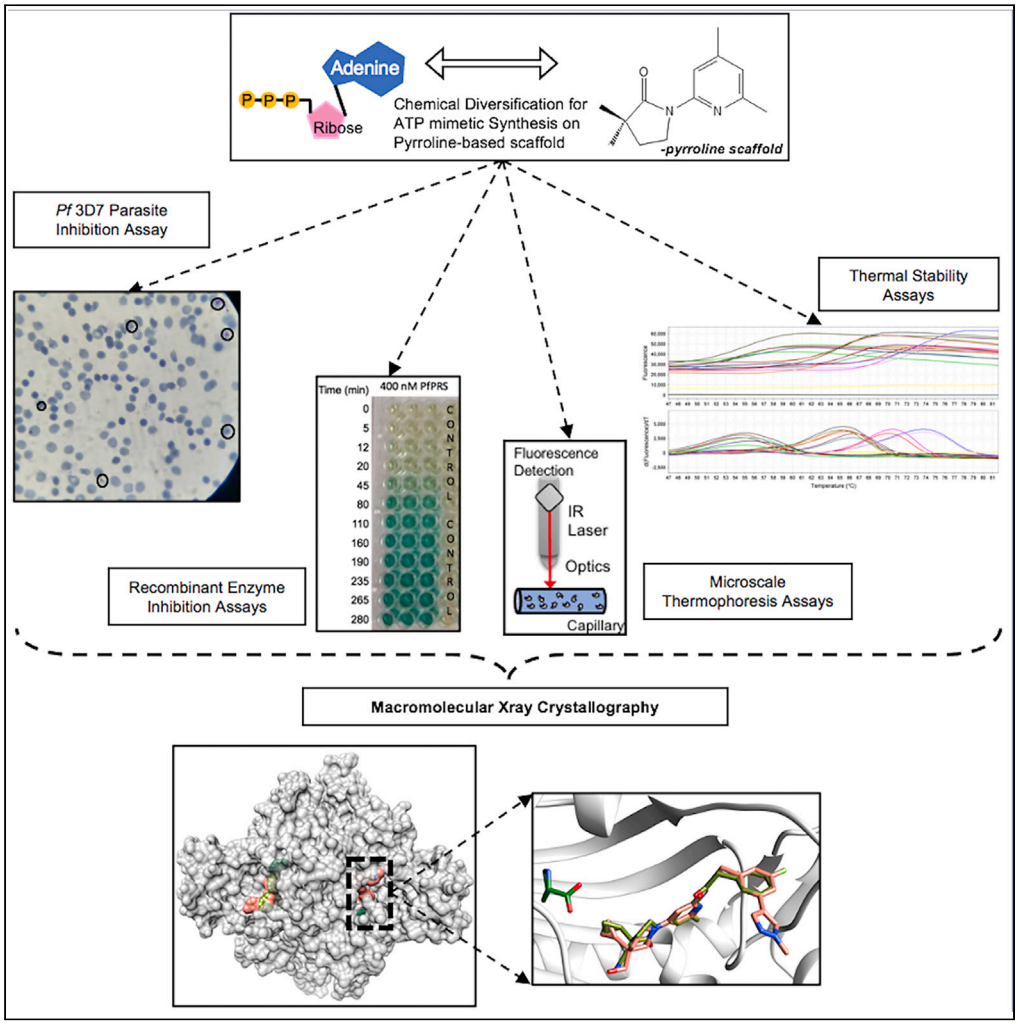

Siddhartha Mishra, Nipun Malhotra, Benoît Laleu, Soumyananda Chakraborti, Manickam Yogavel, Amit Sharma

amit.icgeb@gmail.com

Highlights

Drug resistance against known antimalarials propelled a study of ATP mimetics

Cellular potency assays revealed chemical moieties that contribute to potency

Enzyme-inhibitor structures provided basis of binding and drug mechanism

Structure-based drug development (SBDD) efforts can provide leads

Mishra et al., iScience 27, 110049
July 19, 2024
https://doi.org/10.1016/j.isci.2024.110049

iScience

CellPress
OPEN ACCESS

Article

ATP mimetics targeting prolyl-tRNA synthetases as a new avenue for antimalarial drug development

Siddhartha Mishra,[1,2,4] Nipun Malhotra,[1,5,6] Benoît Laleu,[3] Soumyananda Chakraborti,[2,4] Manickam Yogavel,[1] and Amit Sharma[1,7,*]

SUMMARY

The prolyl-tRNA synthetase (PRS) is an essential enzyme for protein translation and a validated target against malaria parasite. We describe five ATP mimetics (L95, L96, L97, L35, and L36) against PRS, exhibiting enhanced thermal stabilities in co-operativity with L-proline. L35 displays the highest thermal stability akin to halofuginone, an established inhibitor of *Plasmodium falciparum* PRS. Four compounds exhibit nanomolar inhibitory potency against PRS. L35 exhibits the highest potency of ~1.6 nM against asexual-blood-stage (ABS) and ~100-fold (effective concentration [EC_{50}]) selectivity for the parasite. The macromolecular structures of *Pf*PRS with L95 and L97 in complex with L-pro reveal their binding modes and catalytic site malleability. Arg401 of *Pf*PRS oscillates between two rotameric configurations when in complex with L95, whereas it is locked in one of the configurations due to the larger size of L97. Harnessing such specific and selective chemical features holds significant promise for designing potential inhibitors and expediting drug development efforts.

INTRODUCTION

Malaria, caused by the apicomplexan parasite Plasmodium, remains a global burden due to morbidity and mortality.[1] Reports of resistant Plasmodium strains emerging toward approved antimalarials, including artemisinin combination therapies (ACTs), remain a threat to malaria control and elimination.[2,3] The likelihood of the plasmodial parasite gaining one or more highly advantageous mutation(s) and overcoming clearance by artemisinin is a significant threat.[4,5] To that end, continuous design and development of next-generation antimalarials with novel mechanisms of action are highly crucial for fighting this infectious disease.

Aminoacyl-tRNA synthetases (aaRSs) are essential enzymes that charge tRNA molecules with their cognate L-amino acid for ribosome processing and protein translation.[6] The aaRSs hold promise as molecular targets since their inhibition stalls protein synthesis. These aaRSs have three druggable catalytic pockets—the amino acid pocket, the ATP pocket, and the 3′-tRNA-binding pocket.[6,7] Additional editing and auxiliary sites also manifest in certain conditions.[6,7] Therefore, inhibition of parasite aaRSs is a promising route for inhibiting parasite growth.[8] Multiple Plasmodium aaRSs have been validated as promising molecular targets, and several inhibitors have been identified.[9–27] Prolyl-tRNA synthetase (PRS), a member of the aaRSs enzyme family that charges amino acid L-proline to its cognate tRNA, has been extensively explored as a target. Halofuginone (HFG), an established inhibitor of Plasmodium and human PRSs, has been shown to have single-digit nanomolar potencies. It is known to block both the L-pro and 3′-tRNA binding pockets, rendering the PRS enzyme inactive.[14,15,18,28,29] Multiple scaffolds, including HFG analogues, that bind to the PRS enzyme's substrate sites, thereby inhibiting enzyme activity, have been reported.[13,18,29–31]

The active site of *P. falciparum* PRS has been explored in several studies.[6,7] Along those lines, the Takeda Pharmaceutical Company Limited designed and derivatized ~300 pyrazinamide- and pyrrolidine-based compounds to specifically target the ATP pocket of PRS from *Homo sapiens*.[30,32] Subsequently, cell-based inhibition activities from the same library against *P. falciparum* 3D7 cell lines were reported.[33] Tye et al. explored the pyrazinamide scaffold to derivatize multiple molecules that were highly potent against the asexual blood stage (ABS) of *Pf*.[27] They designed compounds utilizing the pyrazinamide and HFG scaffold with linkers that bind simultaneously to all three druggable pockets of Plasmodium PRS with high affinity. Many groups have been working on synergistic/antagonistic tandem inhibitor combinations, which were discussed in patent documentation as early as 2019. There is an interest in inhibiting an enzyme by blocking all catalytic

[1]Molecular Medicine – Structural Parasitology Group, International Centre for Genetic Engineering and Biotechnology (ICGEB), Aruna Asaf Ali Marg, New Delhi 110067, India
[2]ICMR-National Institute of Malaria Research (NIMR), Dwarka, New Delhi 110077, India
[3]Medicines for Malaria Venture (MMV), International Center Cointrin (ICC), Route de Pré-Bois 20, 1215 Geneva, Switzerland
[4]Academy of Scientific and Innovative Research (AcSIR), UP, India
[5]Present address: Department of Surgery, Division of Cardiac Surgery, The Ohio State University, Columbus, Ohio, USA
[6]Present address: The Dorothy M. David Heart and Lung Research Institute, The Ohio State University, Columbus, Ohio, USA
[7]Lead contact
*Correspondence: amit.icgeb@gmail.com
https://doi.org/10.1016/j.isci.2024.110049

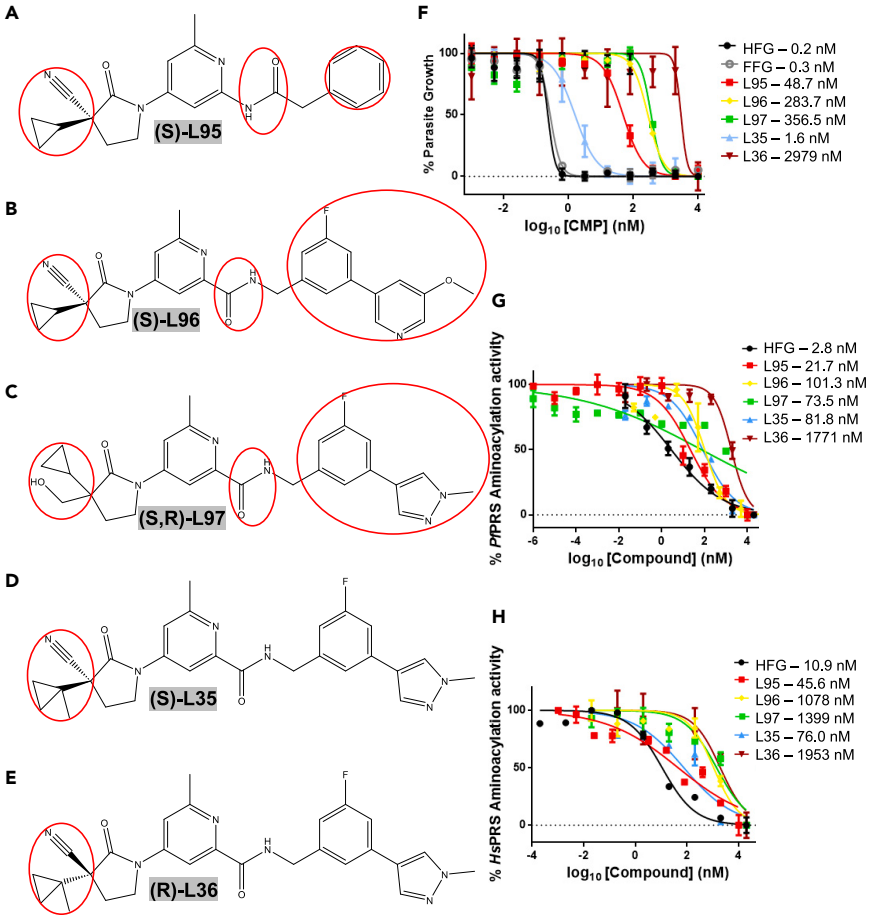

Figure 1. Inhibition profiles of novel ATP mimetics against asexual blood stage of *Plasmodium falciparum* (*Pf*) and recombinantly purified *Homo sapiens* (*Hs*) and *Pf* prolyl-tRNA synthetases (PRSs)

(A–E) The chemical structures of 1-(pyridin-4-yl) pyrrolidin-2-one scaffold derivatives L95, L96, L97, L35, and L36 are shown. The red circles highlight the unique defining moieties of the compound from the other compounds within this group.

(F–H) Dose-response parasite inhibition assays performed on the asexual blood stage of *Pf* against halofuginone (HFG), febrifugine (FF), and the ATP mimetics (L95, L96, L97, L35, and L36) (F). Aminoacylation activity inhibition assays performed for HFG and the ATP mimetics (L95, L96, L97, L35, and L36) against (G) *Pf* and (H) *Hs* PRSs are also shown. The dose-dependent sigmoidal curves were used to calculate EC_{50} (for F)/IC_{50} (for G and H) values for each compound in at least two independent biological replicates with three technical replicates each. Error bars represent mean ± SD.

sites within it. This aligns with our previous work relating to the double-drugging of *Toxoplasma gondii* PRS (apicomplexan intracellular parasite responsible for toxoplasmosis), which served as a proof-of-concept for simultaneous targeting of multiple pockets (STOMP), an attractive paradigm for anti-infective therapeutic development.[29]

In this study, we have investigated the pyrrolidine-based ATP mimetic parent scaffold—L95, and four of its derivatives (L96, L97, L35, and L36) against the plasmodial and human PRSs, and against the ABS of *P. falciparum* (Figure 1).[33] Our data show that all five ATP mimetics independently bind to parasite and human PRSs by making stable complexes, particularly in the presence of L-pro (Figure 2; Table 1). All five mimetics inhibit *Pf*PRS potently, and four compounds exhibit nanomolar inhibitory concentration (IC_{50}) values. L97 is more selective toward *Pf*PRS than *Hs*PRS (Tables 2 and S1). L35 was observed to be the most selective and potent against the malarial parasite, followed by L95 according to SI-EC_{50} (Tables 2 and S2). We also present two high-resolution crystal structures of *Pf*PRS in complex with L95 and L97, both in the presence of L-pro. The structures elucidate the specific molecular interactions that may drive their selectivity and potencies. Binding affinities (K_ds) of the compounds were measured by microscale thermophoresis (MST) and provided a window for understanding drug binding efficacies (Figure 3; Tables 2 and 3). Thus, our work paves the path to more potent and selective drug design and development efforts against malaria.

RESULTS

All five novel ATP mimetics bind to *Pf*PRS, making stable complexes

For comparisons within a protein-substrate-inhibitor system, ΔT_m from the protein's apo form (the reference T_m) aids in determining relative thermal stability. Our analysis revealed that all five ATP mimetics (L95, L96, L97, L35, and L36) individually bind to both *Pf* and *Hs* PRSs, giving

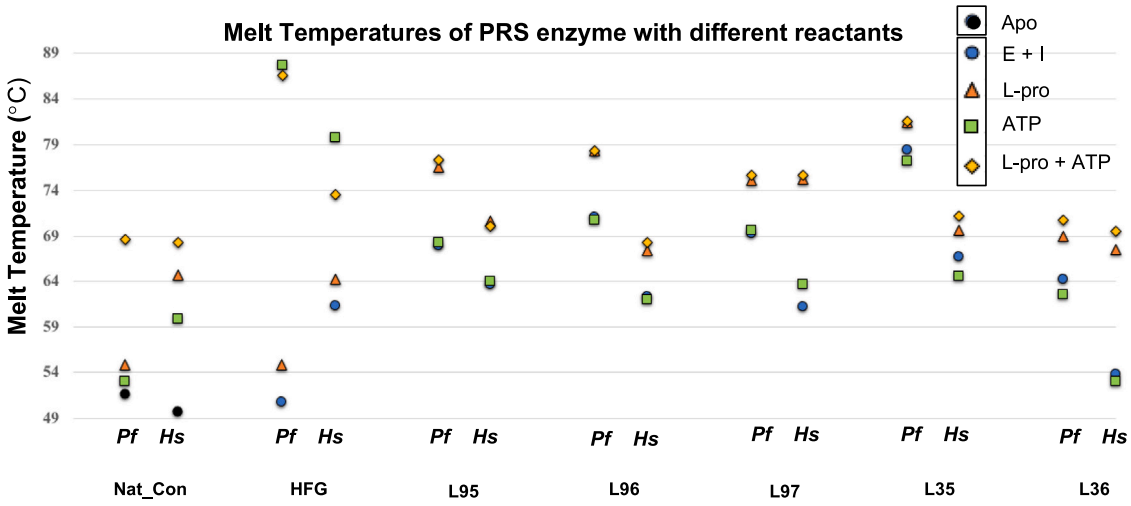

Figure 2. PRS melt profiles with different reactants.

Thermal shift assays were performed to evaluate the melt temperatures of *Pf*PRS and *Hs*PRS in 7 groups i.e., in addition to natural conditions (Nat_Con), and also with the ligands HFG, L95, L96, L97, L35, and L36. These were computed in "Apo condition" (black circle), "Enzyme + Inhibitor (E + I)" condition (blue circle), in presence of L-pro condition (coral triangle), in presence of ATP condition (green square), and in presence of both L-pro and ATP condition (yellow diamond). For exact Tm values, please refer to Table 1 and Figure S3.

rise to thermally stable complexes, albeit the complexes with *Pf*PRS tend to be comparatively more stable than with *Hs*PRS (Figures 2 and S2; Table 1). Further, the presence of L-pro makes the enzyme-substrate-compound complexes comparably or more thermally stable with both *Hs*PRS and *Pf*PRS (Figures 2 and S2; Table 1). L35 with both *Pf*PRS and *Hs*PRS is ~3° more stable in the presence of L-pro, whereas L36 is about 4.7° and 13.7° more stable, respectively (See Table 1).

The thermal shift assays (TSAs) reveal that L35 displayed the best thermal stability in complex with *Pf*PRS in the presence of L-pro + ATP, matching close to HFG, which is an established inhibitor of PRSs that binds to the L-pro and tRNA binding sites (ΔT_m-$HFG_{Pf:\ L\text{-}pro+ATP}$ = 34.9, ΔT_m-$L35_{Pf:\ L\text{-}pro+ATP}$ = 29.8). On the other hand, L97 showed better stability with *Hs*PRS in the presence of both natural ligands (ΔT_m-$HFG_{Hs:\ L\text{-}pro+ATP}$ = 23.7, ΔT_m-$L97_{Hs:\ L\text{-}pro+ATP}$ = 25.9) (Figure 2; Table 1). The least thermally stable complexes with *Pf*PRS individually were of HFG and L36 (ΔTm-HFG_{Pf} = 1.0, ΔTm-$L36_{Pf}$ = 12.6), while in the presence of both natural ligands it was L36 (ΔTm-$L36_{Pf:\ L\text{-}pro+ATP}$ = 19.1) (Table 1). These were tested in Enzyme:Compound ratio of 1:50 in molar terms. Higher compound ratios give higher Tms as reported earlier.[15,16] In the case of *Hs*PRS, similar to *Pf*PRS, L36 forms the most minor thermally stable complex individually (ΔTm-$L36_{Hs}$ = 4.0), but it is closely followed by L96 when in the presence of both natural ligands (ΔTm-$L96_{Hs:\ L\text{-}pro+ATP}$ = 18.5, ΔTm-$L36_{Hs:\ L\text{-}pro+ATP}$ = 19.7). Such thermal stability profiles of L35 and L36 are particularly interesting, considering that both are enantiomers.

L96 displayed the highest binding affinity to both PRSs (K_ds of 87.5 and 4.7 nM for the *Pf* and *Hs* PRSs, respectively, determined via MST) (Figure 3; Tables 2 and 3). L95 has a K_d of ~278 nM with the *Pf* enzyme but that of 28 nM against the *Hs* enzyme. L97 and L36 have the least binding affinities to the human enzyme, i.e., that of ~2288 nM and 1478 nM. Interestingly, SI-K_d values reveal L97 and L36 to be the most and second-most selective toward the parasite (L97-SI-K_d = 10.3, L36-SI-K_d = 3.8), albeit both of them are not that much more selective only based on thermal profiles (see Figures 2 and 3; Tables 1, 2 and 3).

Table 1. *Pf*PRS and *Hs*PRS melting temperatures (Tm)

	Pf	*Hs*	*Pf*	*Hs*	*Pf*	*Hs*	*Pf*	*Hs*
CMP	*Apo*	*Apo*	L-pro	L-pro	ATP	ATP	L-pro + ATP	L-pro + ATP
	51.7 (0.0)	*49.8 (0.0)*	54.7 (3.1)	64.7 (14.9)	53.0 (1.3)	59.9 (10.1)	68.6 (16.9)	68.3 (18.5)
HFG	50.7 (1.0)	61.4 (11.6)	54.7 (3.1)	64.3 (14.5)	87.7 (36.0)	79.8 (30.1)	86.6 (34.9)	73.5 (23.7)
L95	67.9 (16.2)	63.7 (13.9)	76.5 (24.9)	70.6 (20.8)	68.3 (16.6)	64.1 (14.3)	77.3 (25.6)	70.1 (20.3)
L96	71.1 (19.4)	62.4 (12.6)	78.4 (26.7)	67.4 (17.7)	70.8 (19.1)	62.0 (12.2)	78.3 (26.6)	68.3 (18.5)
L97	69.2 (17.6)	61.2 (11.4)	75.1 (23.4)	75.2 (25.5)	69.7 (18.0)	63.7 (13.9)	75.7 (24.0)	75.6 (25.9)
L35	78.5 (26.8)	66.7 (17.0)	81.5 (29.8)	69.6 (19.8)	77.2 (25.5)	64.6 (14.9)	81.5 (29.8)	71.2 (21.4)
L36	64.2 (12.6)	53.8 (4.0)	69 (17.3)	67.5 (17.7)	62.6 (10.9)	53.0 (3.2)	70.8 (19.1)	69.5 (19.7)

All values have been rounded off to the nearest significant value after first decimal. Values in parentheses are the difference in temperature from the reference Apo Tm values (italicized): *Pf*PRS – 51.7°C, *Hs*PRS – 49.8°C.

Table 2. Summary of all IC_{50}, EC_{50}, and $K_{d\text{-}mean}$ values with the respective SI values on the basis of each parameter

CMP	*Pf*-IC_{50} (nM)	*Hs*-IC_{50} (nM)	SI-IC_{50}	*Pf*-EC_{50} (nM)	*Hs*-CC_{50} (ARPE19/MDA231) (nM)	SI-EC_{50}	K_d-*Pf* (nM)	K_d-*Hs* (nM)	SI-K_d
HFG	2.8	10.9	3.9	0.2	ND/ND	ND/ND	73.8	53.2	0.7
L95	21.7	45.6	2.1	48.7	672/382	13.8/7.8	277.8	28.0	0.1
L96	101.3	1078	10.6	283.7	783/393	2.8/1.4	87.5	4.7	0.1
L97	73.5	1399	19.0	356.5	1120/3600	3.1/10.1	221.7	2288.1	10.3
L35	81.8	76.0	0.9	1.6	295/134	185.5/84.3	288.1	123.7	0.4
L36	1771	1953	1.1	2763	ND/ND (>2 uM)	ND/ND	393.4	1478.0	3.8

All values have been rounded off to the nearest significant value after first decimal.

L95, L96, L97, and L35 inhibit *Pf*PRS at nanomolar concentration

We assessed the potency of all five compounds against *Pf*PRS and *Hs*PRS using enzyme inhibition assays . Since aminoacylation is a two-step reaction, we studied the aminoacyl-adenylate complex formation and measured the release of pyrophosphate (PPi) via a malachite green dye-based assay. The measured half-maximal inhibitory concentration (IC_{50}) values for individual inhibitors L95, L96, L97, L35, and L36 are shown in Figures 1F and 1G for *Pf*PRS and *Hs*PRS. HFG was used as a positive control to assure assay fidelity, considering it is an established *Pf*PRS inhibitor.[13,31] The high potency of four of the five inhibitors (L95, L96, L97, and L35; except L36) is evident from their nanomolar IC_{50} values for *Pf*PRS (Figure 1F). L95 is the most potent against *Pf*PRS compared to *Hs*PRS (Figure 1; Tables 2 and S1). Furthermore, L96 (SI-IC_{50} = 10.6) and L97 (SI-IC_{50} = 19.0) were discernibly selective toward *Pf*PRS compared to the human counterpart *in vitro*, with L97 being the most selective (Tables 2 and S1). L35 and L36 remain comparably non-specific, with SI-IC_{50} being ~1, although L35 is nearly 20 times more potent than L36 against both *Pf* and *Hs* PRSs (Tables 2 and S1).

L95, L96, L97, and L35 in-cellular inhibition observed against parasite and mammalian cells

We assessed the *in-cellulo* potency of L95, L96, L97, L35, and L36 in addition to HFG, febrifugine (FF), chloroquine (CQ), and dihydroartemisinin (DHA), which were used as controls. As expected, HFG is the most potent of all inhibitors screened. L35 is the most potent and selective toward the parasite among the ATP mimetics, with an effective concentration (EC_{50}) of ~1.6 nM against *Pf* 3D7 culture and cytotoxic concentration (CC_{50}) values of 295 nM and 134 nM against ARPE19 and MDA231 cell lines, respectively (Figure 1; Tables 2 and S2). L95 is the second most potent and selective among the ATP mimetics after L35, with an EC_{50} of 48.7 nM and CC_{50} values of 672 nM and 382 nM (see Figure 1; Tables 2 and S2). Furthermore, although L96 is more potent than L97, it is more selective toward the parasite (SI-EC_{50} = 2.8 and 1.4 of L96 vs. 3.1 and 10.1 of L97, Tables 2 and S2). In line with the enzyme binding and inhibition analyses, L36 exhibited no significant inhibitory effect on the parasitic or mammalian cell lines up to 2 μM.

Structural intricacies in *Pf*PRS complexes with L95 and L97 in the presence of L-pro

To elucidate the structural basis of binding modes of ATP mimetics, assess the apparent higher thermal stability in the presence of L-pro, and reveal insights into selectivity between the *Pf*PRS and host *Hs*PRS, we attempted to co-crystallize *Pf*PRS with all five compounds in the presence of L-pro. We successfully obtained crystals for L95-bound *Pf*PRS (*Pf*PRS-L-pro-L95) and L97-bound *Pf*PRS (*Pf*PRS-L-pro-L97) in Morpheus A9 and E11, respectively (Table 4). One *Pf*PRS-L-pro-L95 monomer crystallized in the P 3_2 2 1 space group, while *Pf*PRS-L-pro-L97 two dimers crystallized in P 2_1 2_1 2_1. The superposition of 494 Cα-atoms of the two chains of AB dimer of L97-bound *Pf*PRS shows a root-mean-square deviation (RMSD) of 0.5–1 Å. The RMSD between 494 Cα-atoms of chains A of *Pf*PRS-L-pro-L95 and *Pf*PRS-L-pro-L97 monomer is low at 0.2–0.4 Å. The temperature factors reveal that the structures are well-ordered and display low mobility (Table 4). These structures showed that ATP has a much more connected interaction network around its binding shell than either L95 or L97 (see Figures S2, 4C, and 4D).

Structural analysis of *Pf*PRS-L-pro-L95 reveals L-pro bound in the amino acid pocket and L95 binding in the ATP pocket as it interacts with *Pf*PRS via multiple hydrophobic interactions, a pi-pi stacking interaction with Phe405 of *Pf*PRS, three hydrogen bond interactions with the side chain and main-chain atoms, and one water-mediated interaction with Arg390 (Figure 4C). *Pf*PRS-L-pro-L97 displays a highly similar interaction profile with *Pf*PRS except for two additional interactions with Arg403—one pi-cation interaction and a hydrogen bond by the presence of its fluorinated moiety (see Figure 4D). This added interaction degree could account for L97's high potency against *Pf*PRS.

Figure 5A shows L95 and L97 bound within the *Pf*PRS protomer. As in Figure 5B, L97 fills up additional free space beyond L95 such that a snug fit is achieved for the complex. For this, L97 induces rotameric displacements of Glu392, Lys394, Arg401, and Arg403 (Figure 5C). Arg401 seems to oscillate between two rotameric positions (wide-open and closed-locked) when *Pf*PRS is bound to L95, but in complex with L97, it gets locked into only the closed-locked position due to the steric hindrance by the 3-methylpyrazole moiety of L97 (Figure 5). Arg390 and Lys394 also move outwards to accommodate the larger L97 molecule. Arg403, on the other hand, moves closer to the compound by the two additional interactions it makes with L97 in contrast to L95. These rotameric configurations encourage the compounds to enter, fit in, and sit well within the ATP pockets of these enzymes.

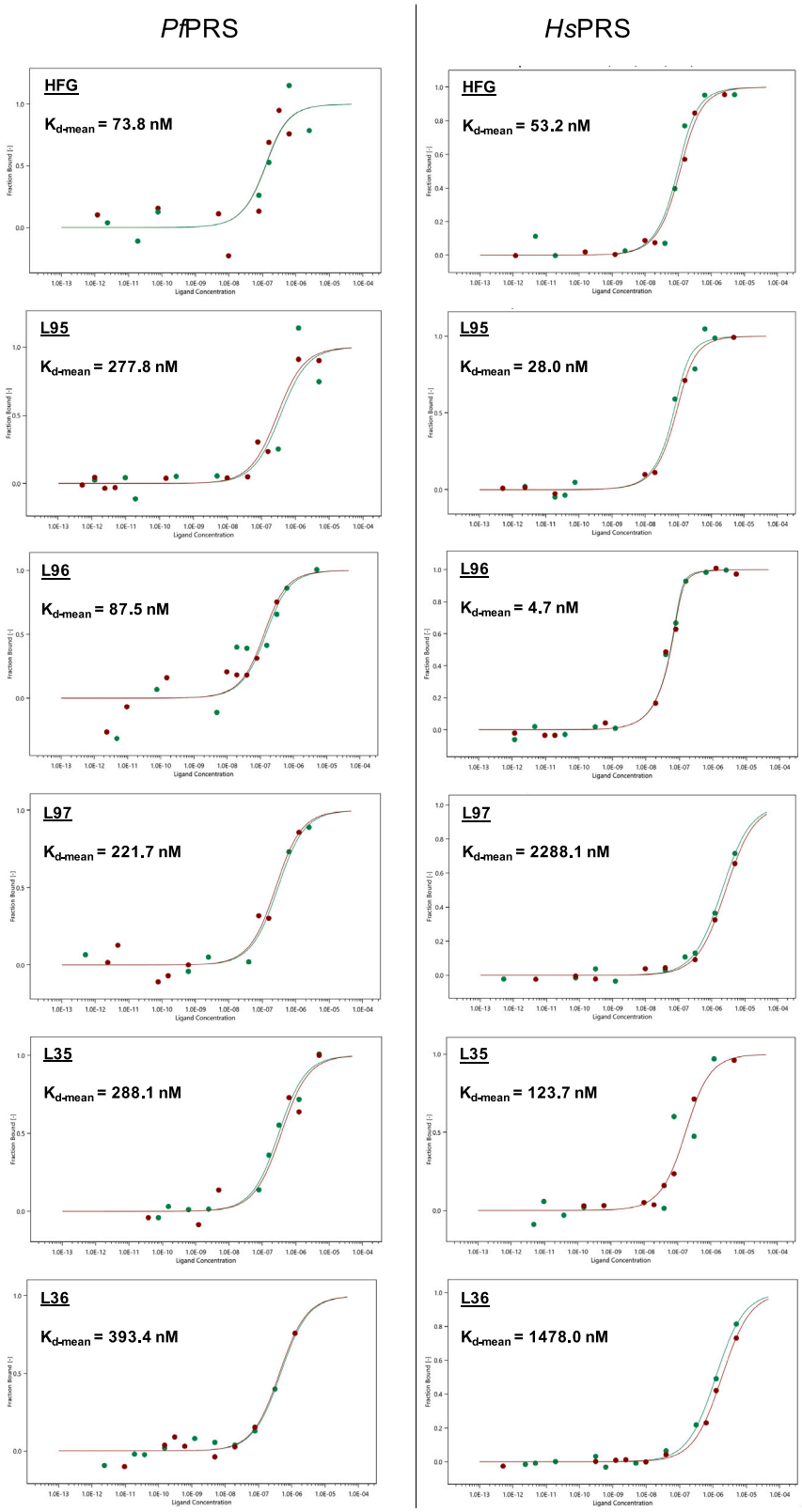
PfPRS
HsPRS
HFG
Kd-mean = 73.8 nM
HFG
Kd-mean = 53.2 nM
L95
Kd-mean = 277.8 nM
L95
Kd-mean = 28.0 nM
L96
Kd-mean = 87.5 nM
L96
Kd-mean = 4.7 nM
L97
Kd-mean = 221.7 nM
L97
Kd-mean = 2288.1 nM
L35
Kd-mean = 288.1 nM
L35
Kd-mean = 123.7 nM
L36
Kd-mean = 393.4 nM
L36
Kd-mean = 1478.0 nM
Fraction Bound [-]
Ligand Concentration

Figure 3. Binding affinity determination via microscale thermophoresis (MST)

Analyses for K_d determination of compounds involved in this study was done via MST using the Monolith Analysis Nano Temper Software. Unlabeled ligands HFG, L95, L96, L97, L35, and L36 were titrated into a fixed concentration (100 nM) of labeled *Pf*PRS (left column) and *Hs*PRS (right column) in the presence of 100 nM L-proline and 1 μM ATP in two independent replicate experiments (n = 2). Computed $K_{d\text{-mean}}$ values are shown alongside each dose-response curve in bold. For individual Kd and statistical parameters, please refer to Table 3.

Selectivity of L95 and L97 toward *Pf*PRS based on structural features with *Hs*PRS

Our selectivity analyses reveal L97 to be the most selective toward *Pf*PRS when compared to *Hs*PRS (Figures 1F and 1G; Tables 2 and S1). Only L97 was identified as selective toward *Pf*PRS among the other compounds tested. To explore the structural basis of the selectivity of L95 and L97, we aimed to compare their interaction profiles in complexes with *Pf*PRS and *Hs*PRS. Our group recently communicated work on another intracellular parasite, *Toxoplasma gondii* (*Tg*) PRS, wherein the same novel ATP mimetics were explored and described via structural complexes with both *Tg*PRS and *Hs*PRS.[34] The overall folds of the *Pf* and *Hs* PRS dimers were similar to those in previously reported structures.[13–15,17,18,29,35] Utilizing the *Hs*PRS complexes with L95 and L97 from our previously communicated study, we used structural comparisons between *Pf* and *Hs* complexes.

Intriguingly, Thr478 (Thr1240 in *Hs*) is seen in two rotameric conformations—the hydroxyl group facing the ligand in *Pf* is in contrast to it facing away in *Hs* (see Figures 4C, 4D, 6A, and 6B). In addition to rotameric differences, the interaction profiles of L95 in *Pf*PRS-L-pro-L95 and *Hs*PRS-L-pro-L95 are identical except for an additional water-mediated hydrogen bond between the phenylacetamide moiety of L95 and Arg390 of PRS in *Pf*PRS-L-pro-L95 which is absent in the *Hs* complex (Figures 4C, 4D, and 6A). This extra hydrogen bond could explain the higher potency of L95 against *Pf*PRS compared to *Hs*PRS. Arg401 (Arg1163 in *Hs*) is seen in two rotameric configurations (wide-open and closed-locked [as in *Pf*PRS-L-pro-L97]) in *Pf*PRS, but in *Hs*PRS, only the wide-open conformation of Arg1163 (Arg401 in *Pf*) is observed. *Hs*PRS interacts with L95 also by Pro1158 (Pro396 in *Pf*) and Arg1278 (Arg514 in *Pf*) as well (see Figure 6A).

Furthermore, L97 makes three additional hydrogen bonds with Glu1154, Gln1237, and Arg1278 in *Hs*PRS-L-pro-L97 (Figure 6B). This scenario would make L97 a better inhibitor with stronger binding; however, it lacks the pi-cation interaction and the hydrogen bond with Arg1165 in *Hs*PRS, as seen with Arg403 in *Pf*PRS-L-pro-L97 (Figure 6B). This indicates a better binding of L97 to *Pf*PRS—although melt temperature values reveal thermal stability and selectivity tending toward *Hs*PRS (Figure 2). Moreover, Arg401 in *Pf*PRS (Arg1163 in *Hs*) appears to have a more closed-locked conformation, which might be another reason for its more thermally stable complex (Figures 2 and 6B). These data correlate with the relative thermal stability of complexes and enzyme inhibition assays.

Pyrrolidine-based vs. pyrazinamide-based ATP mimetics

NCP26 and other pyrazinamide-based ATP mimetics recently described by Tye et al. exhibit sub-micromolar potencies against the ABS of *Pf*.[27] Notedly, NCP26, 34, 35, 36, and 40 are highly potent, evident from their EC_{50} values of 67.4 nM, 6.8 nM, 18.7 nM, 18.7 nM, and 21.9 nM (Table S3). Furthermore, they bind with high affinities, but they also encounter similar selectivity concerns as with the pyrrolidine-based ATP mimetics described in this study (see Table S3). L35 remains the most potent against ABS of *Pf* at an EC_{50} of ~1.6 nM among all these inhibitors. None of the most potent inhibitors described from the two chemotypes, pyrazinamides or pyrrolidines, exhibit more than 100× selectivity. However, an interesting observation is that pyrrolidines seem more selective toward *Pf* than pyrazinamides, as indicated by the cellular, enzymatic and K_d-based SI values (Tables 2 and S1–S3).

Regarding the resistance-conferring mutations for these two chemotypes, we compared the crystal structure determined binding sites of the most potent derivatives of both scaffolds in mutant lines generated in *Pf* for the pyrazinamide scaffold (NCP26) and *Tg* for the pyrrolidine scaffold (L35) as described by Tye et al. and Manickam et al. previously.[27,34] For NCP26, the mutants generated included PRS variants *Pf*PRS-F405L and *Pf*PRS-T512S, while for L35, *Tg*PRS-T477A and *Tg*PRS-T592S mutants were accounted for (see Figure 6). There is high conservation in the ATP binding (9 of 10) and L-pro binding (5 of 6) residues between the *Pf* and *Tg* PRSs (see Figure S1). Interestingly, the *Pf*PRS-F405L mutant had a copy number variation of ~3-fold amplification with 1 mutant and 2 wild-type (WT) alleles, which was not the case in the *Pf*PRS-T512S mutant.[34] For

Table 3. Statistical and K_d parameters of HFG, L95, L96, L97, L35, and L36 with *Hs* and *Pf* PRSs

S. No	CMP	K_d-*Pf* (nM) (n = 1, 2)	[a]RA	[b]SER	[c]STN	K_d-*Hs* (nM) (n = 1, 2)	[a]RA	[b]SER	[c]STN
1	HFG	74.8, 72.9	9.8, 6.7	1.9, 1.2	6.3, 6.6	42.4, 61.9	11.2, 50.7	0.6, 2.0	22.5, 30.4
2	L95	312.7, 242.9	8.2, 26.9	1.7, 1.9	5.6, 15.7	20.8, 35.2	10.1, 46.0	0.8, 1.1	14.7, 49.5
3	L96	96.4, 78.6	8.0, 8.4	1.7, 1.4	5.4, 7.3	4.0, 8.2	6.7, 12.9	0.2, 0.7	43.2, 20.6
4	L97	242.7, 200.7	9.3, 7.2	0.7, 0.7	17.2, 12.0	1994.7, 2581.4	17.4, 35.0	0.5, 0.9	39.5, 46.1
5	L35	258.1, 318.2	7.5, 12.3	0.5, 1.7	18.8, 9.2	123.8, 123.7	11.4, 7.6	2.1, 0.3	6.4, 28.0
6	L36	412.5, 374.3	26.9, 10.4	1.5, 0.7	21.0, 17.5	1164.8, 1791.1	20.1, 50.0	0.5, 0.9	46.0, 61.5

All values have been rounded off to the nearest significant value after first decimal.

[a]RA, Response Amplitude (RA).

[b]SER, Standard error of regression.

[c]STN, Signal to noise.

Table 4. Summary of data collection and refinement statistics

	*Pf*PRS-L-pro-L95	*Pf*PRS-L-pro-L97
PDB code	7F96	7F97
Data collection		
Space group	P 3_2 2 1	P 2_1 2_1 2_1
Cell dimensions		
a, b, c (Å)	103.61, 103.61, 128.04;	82.02, 140.60, 187.09;
α, β, γ (°)	90.0, 90.0, 120.0	90.0, 90.0, 90.0
Resolution (Å)	48.02–2.58 (2.64–2.58)	93.77–2.25 (2.31–2.25)
I/σI	26.1 (3.7)	8.4 (1.8)
Completeness (%)	99.4 (92.5)	100 (100)
Redundancy	19.5 (17.1)	13.2 (13.5)
CC1/2 (%)	100 (90.0)	99.0 (99.6)
No. of unique reflection	25534 (1720)	104091 (7634)
Refinement		
Resolution (Å)	38.54–2.57 (2.67–2.57)	41.90–2.39 (2.42–2.39)
No. of reflections/test set	25460/1273	85960/4298
Rwork/Rfree (%)	15.5/19.1	17.5/23.2
No. of modeled protein residues	487	487 + 481 + 478 + 475
Total no. atoms	4057	16025
Protein/Water	3949/72	15772/56
Ligand (non-H atoms) L95/L97 + L-Pro	36 (28 + 8)	172 (35 + 8, 35 + 8, 35 + 8, 35 + 8)
Ions/Solvent molecules[a]	0/0	11/14
Average B-factors (Å^2)	62.0	74.0
RMSD		
Bond lengths (Å)	0.007	0.006
Bond angles (°)	0.955	0.874
Ramachandran plot		
Favored/Allowed/Outliers (no of residues) (%)	98 (474)/2 (9)/0 (1)	96 (1828)/3 (64)/1 (5)
Clash score	3	7
Disordered Regions	A – 330–334, 700-704	A – 250–251, 699-706 B – 250–251, 327–335, 701-705 C – 250–251, 328–334, 698-707 D – 250–251, 331–337, 549–552, 698-706

Values in parentheses are for the highest resolution shell.
[a]Ions: Cl and solvent molecules: 1,4-Butanediol and hexane-1,6-diol.

Tg the T592S confers an ~3× drop in parasite susceptibility to L35 while T477A confers an ~6× drop (L35-EC_{50}: WT—27 nM, T477A—186 nM, and T592S—76 nM).[34] Additionally, T477A variant lines exhibit growth impairment, demonstrating a trade-off mechanism the parasite utilizes for drug pressure relief.[34] The corresponding threonines 512 and 592 in *Pf* and *Tg* mutate to serine 512 and 592 (see Figure 7).[34] This loss of the methyl substituent on the residue's beta carbon might be causing the compound to "lock in and bind" less. This is more pronounced in the relative positions of the mutated residues (Figure 7). Via performing interaction analysis on *in-silico* mutated proteins, it was observed that the F405L mutant causes a loss of the pi-pi stacking interaction between the 6-methylpyridine and piperazine cores of L35 and NCP26. The T512S/T592S mutation also perturbs the H-bond network around the compound—as the change to serine causes a decrease in H-bonds that the O-atom makes from 4 in the case of threonine to 2. The lost H-bond interactions in the case of serine are the ones with the main chain N-atoms of T593 and R594 in the *Tg* enzyme.

DISCUSSION

The aaRSs have progressed into molecular targets for many diseases due to their essential nature to accomplish protein translation and highly conserved evolutionary relationships.[6,36–39] The multiple pockets in the active sites within aaRSs enable multiple targeting and allow for the

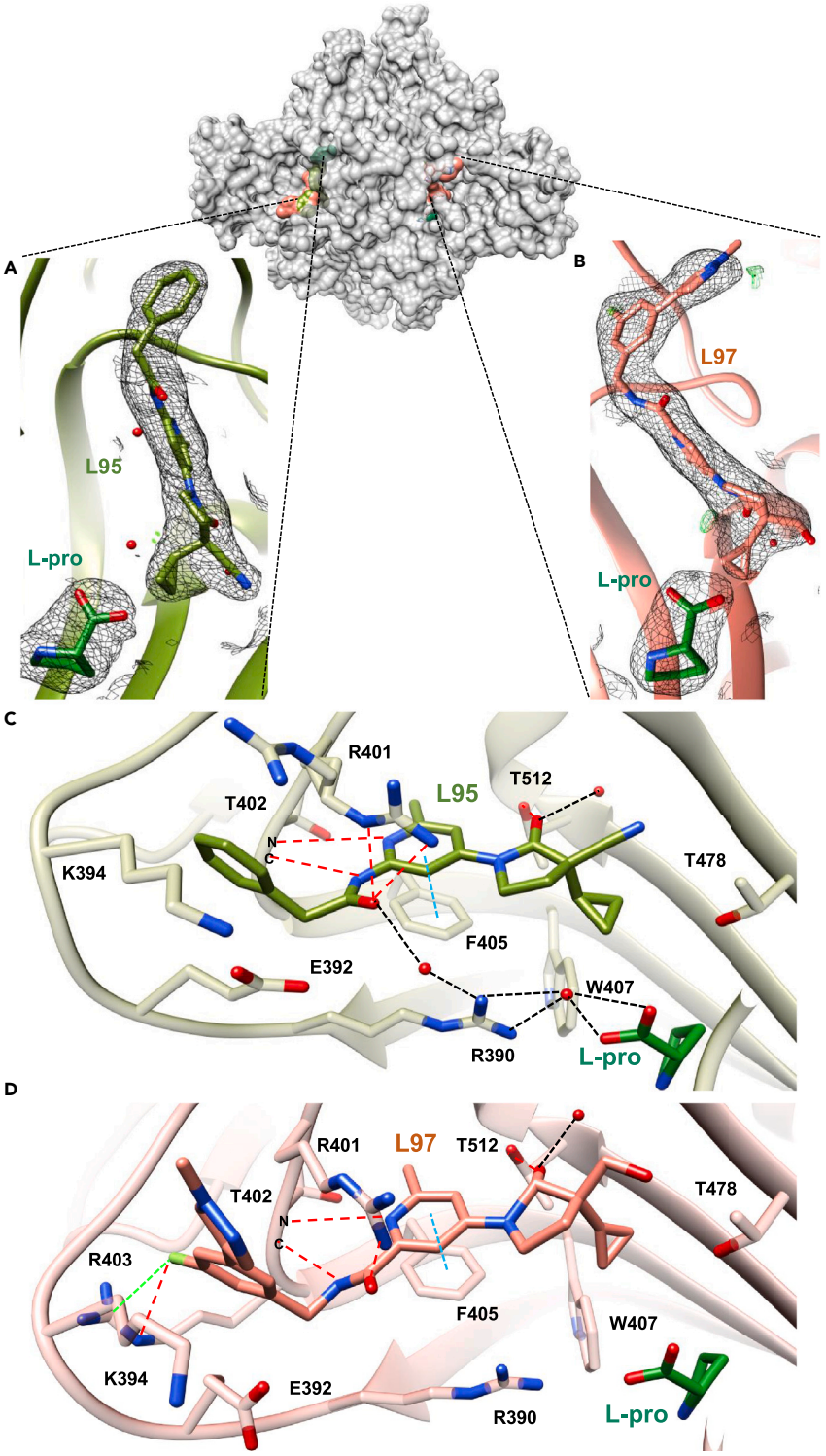

Figure 4. Structural interactions made by L95 and L97 with *Pf*PRS

A molecular surface representation of the *Pf*PRS dimer is shown in the center of the montage—with the protein surface (gray) and the ATP binding sites wherein L95 (olive drab) and L97 (salmon) bind are visible.

Figure 4. *Continued*

(A and B) Composite omit maps generated at ~2.6 Å and 2.4 Å resolution, contoured at 1.5 σ, show bound L95 (olive drab) and L97 (salmon) respectively with L-pro (forest green), confirming their presence in the ATP binding site within *Pf*PRS.

(C and D) Molecular interactions made by L95 (olive drab) (C) and L97 (salmon) (D) with *Pf*PRS are also displayed. Dashed black lines depict water-mediated interactions, cyan depicts pi-pi stacking interactions, and green points to the pi-cation interactions, while the dashed red lines show the hydrogen bond interactions. Bonds with main-chain N/carbonyl groups are depicted by a capital N/C on the ribbon representation.

selective design of inhibitors, as some of these pockets consist of organism-specific features revealed upon deeper structural scrutiny.[16,17] Along these lines, many existing inhibitors of aaRSs are essentially natural substrate-competitive compounds.[8,23,40,41] ATP mimetics are one such class of promising compounds that can be explored by targeting the ATP-binding pocket on aaRSs.[30,32,42]

Here, we examined five ATP mimetics (termed L95, L96, L97, L35, and L36) selected from a library of compounds designed by Takeda Pharmaceutical Company Limited against *P. falciparum* and human PRSs (*Pf*PRS and *Hs*PRS) to assess their potency and selectivity as inhibitors. All five mimetics have better binding stability with PRSs in the presence of L-pro (see Figure 2). The L35 and L36 are S and R enantiomers, but L35 has the highest thermal stability with *Pf*PRS—close to that with HFG—while L36 forms the least thermally stable complex. Nevertheless, it is clear that in the presence of substrate L-pro (i.e., when the L-pro pocket is occupied), the complexes with both *Pf*PRS and *Hs*PRS are either comparably or more thermally stable. This scenario indicates a cooperative binding mechanism with *Pf* and *Hs* PRSs in the presence of L-pro for ATP site binders.

Interestingly, in the presence of ATP alone, the stability of the complexes appears to remain constant or erode when compared to stability profiles in the presence of L-pro. Summarily, L35 was the most potent and selective toward the parasite in cell-based assays, followed by L95, which has the highest inhibitory potency against both the *Pf* and *Hs* PRS enzymes. Interaction profiles of L35 and L36 with *Pf*PRS remain currently unexplored due to the lack of diffraction-quality crystals. A particular trend for enantio-preference for the S enantiomer compared to the R one is manifested in the case of the L35-L36 pair, which warrants further exploration. Structural elucidation via two high-resolution three-dimensional structures of L95 and L97 in complex with *Pf*PRS reveal L97 with two additional interactions with Arg403 of *Pf*PRS. L97 is an interesting compound mainly because it is the most selective against the parasite both in terms of IC_{50} (SI-IC_{50} = 19) and K_d (SI-K_d = 10.3) (see Tables 2, 3, S1, and S2). SI-K_d values also show the least potent compound against the enzyme and ABS of the parasite, L36 (SI-K_d = 3.8), to be the second most selective in terms of K_d

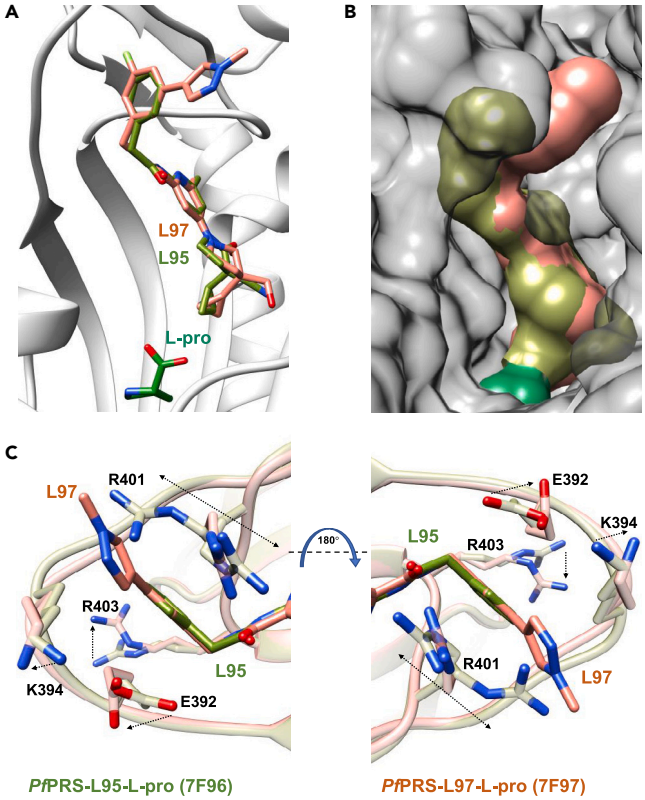

Figure 5. Comparing L95 and L97 bound *Pf*PRS structures

(A and B) An overlay of L95 (olive drab) and L97 (salmon) within the ATP binding pocket in presence of L-pro (forest green) is shown in (A), and (B) shows the same in molecular surface representation depicting the snug fit of the compounds within the protomer catalytic cavity.

(C) The molecular agility exhibited by *Pf*PRS active site to accommodate L95 and L97 in comparison to each other.

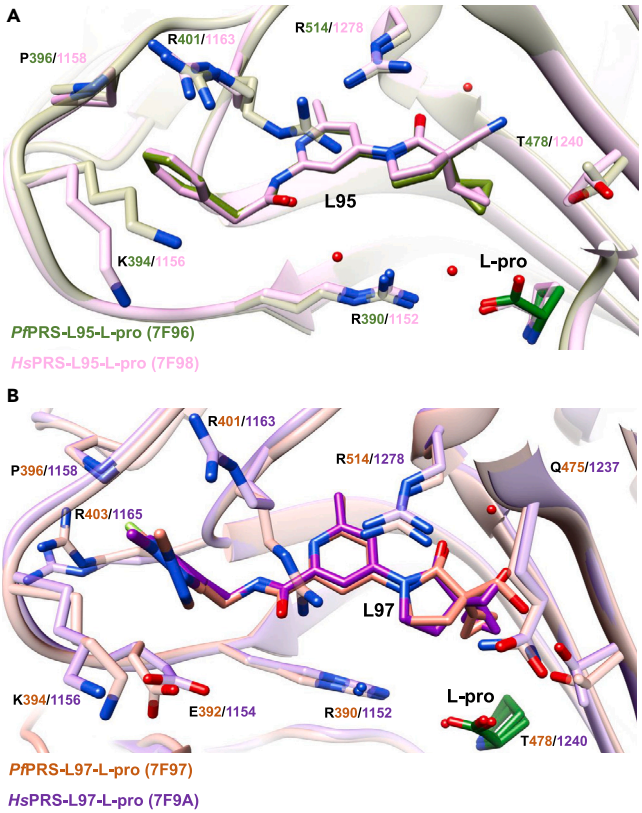

Figure 6. Structural overlay showing distinct active site configurations induced by L95 and L97 among *Pf*PRS and *Hs*PRS

(A and B) An overlay of only the distinct interacting residues among *Pf*PRS and *Hs*PRS with (A) L95 (PDB IDs: 7F96 and 7F98) and (B) L97 (PDB IDs: 7F97 and 7F9A) is shown. Differing side-chain rotameric configurations can be seen.

toward the *Pf* enzyme. In contrast, all other compounds display selectivity toward the human enzyme (see Tables 2, 3, S1, and S2). Intriguingly, L35, which is the most selective in terms of EC_{50} values (185.5/84.2), has a fractional SI-K_d (SI-K_d = 0.4) (Tables 2, 3, S1, and S2).

The ATP-binding pocket, one of the three druggable pockets on aaRSs, is a promising site to target the enzyme, and thus, ATP mimetics hold potential as inhibitors. In this context, it is essential to consider that ATP mimetics can be indiscriminate and have adverse off-site effects. Recently, Adachi et al. designed compounds that competitively bind to the ATP pocket of *Hs*PRS as anti-fibrosis inhibitors.[32,42] Many of those compounds also had anti-plasmodial effects evident from low EC_{50} values, as shown by Okaniwa et al., 2021.[33] The current understanding supported by such evidence suggests that because enzymes recognize ATP by a highly unique and specific molecular mechanism, the possibility of off-site targets of specifically designed ATP mimetics for an enzyme based on a structure can be low for a select few. However, the problem of not achieving orthologous selectivity remains due to the highly conserved pockets for ATP catalysis in the same enzyme in multiple organisms. To achieve selectivity for different scaffolds in the case of PRS and other aaRSs, one could envision derivatizing each scaffold for a particular organism by exploiting subtle structural differences such that a specific core can be worked upon to inhibit that organism specifically. The selectivity distinction between the pathogen and host PRS is paramount for successful drug development efforts, and ATP-mimetics may be a promising option. The possibility of ATP mimetics having the potential to be exploited for designing target-specific and organism-selective tandem inhibitors along with quinazolinone-based inhibitors (QBIs) is encouraging.[29,34] The principles of structure-based targeting of orthologous pathogen proteins (STOPP) and STOMP have the potential to propel current drug design and development efforts to fruition.[16,29]

Limitations of the study

This study lacks malaria model experiments in animals, which would be very informative for understanding the drug-like properties of the compounds studied here. Also, a wider variety of ATP mimetics based on these compounds may have provided better starting points for lead inhibitor development.

STAR★METHODS

Detailed methods are provided in the online version of this paper and include the following:

- KEY RESOURCES TABLE

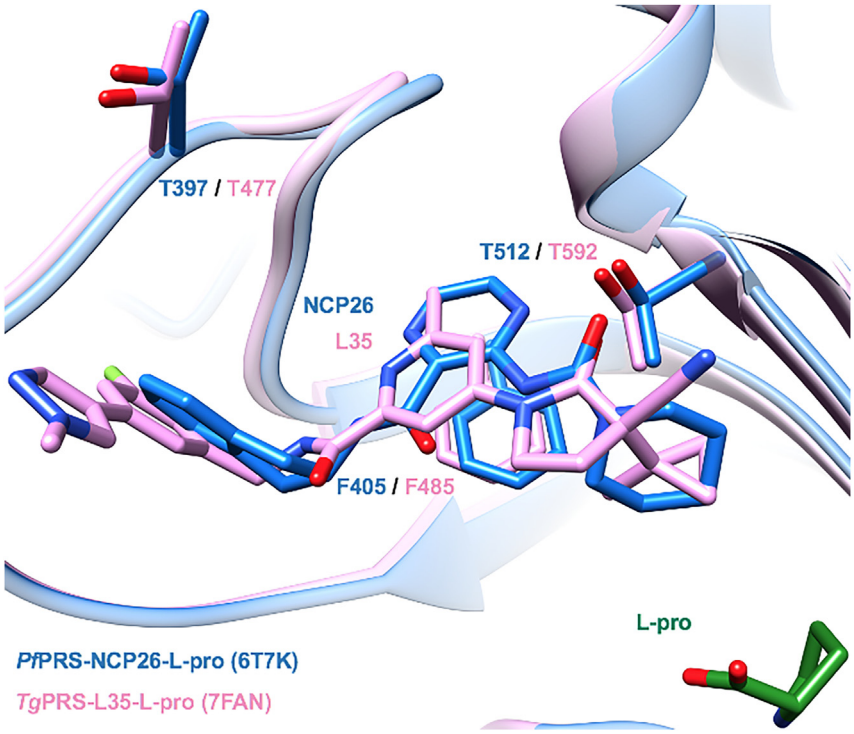

Figure 7. Structural overlay of ATP and L-pro binding pockets of *Pf*PRS-NCP (6T7K) and *Tg*PRS-L35 (7FAN)

An overlay of the ATP and L-pro binding pockets of *Pf*PRS-NCP26-L-pro (PDB ID: 6T7K) (cornflour blue) and *Tg*PRS-L35-L-pro (PDB ID: 7FAN) (pink) is shown. The corresponding resistance-conferring mutating residues have been marked—F405 and T512 which manifest as F405L and T512S in *Pf*PRS while T477 and T592 manifest as T477A and T592S in *Tg*PRS, respectively. The relative confirmations of all three corresponding residues in both structures are shown.

SUPPLEMENTAL INFORMATION

Supplemental information can be found online at https://doi.org/10.1016/j.isci.2024.110049.

ACKNOWLEDGMENTS

We thank Takeda Pharmaceutical Company Limited and MMV for synthesizing the compounds L95, L96, L97, L35, and L36. We acknowledge the support of the UK Medical Research Council (grant MR/V001329/1 awarded to D. I. Stuart). We are grateful for beamtime at the Diamond Light Source (DLS) and the staff of beamline I03 for preliminary data collection (BAG application mx28534). We are also grateful for beamtime at the SOLEIL beamline PROXIMA 1 and the staff of beamlines PROXIMA 1 and PROXIMA 2A for their aid in data collection. We also thank J. Gill for her valuable input in the manuscript preparation. This work was supported by grants from Medicines for Malaria Venture (MMV) (P020/00065) and the Department of Biotechnology (DBT), Government of India (PR32713). J. C. Bose National Fellowship (SB/S2/JCB-41/2013) from the

Department of Science and Technology (DST) supported A.S. S.C. received the Ramalingaswami Fellowship (BT/RLF/Reentry/09/2019) from the Department of Biotechnology, Government of India.

AUTHOR CONTRIBUTIONS

Conceptualization: A.S.; methodology: S.M. and A.S.; validation: S.M., M.Y., and A.S.; formal analyses: S.M. and M.Y.; investigation: S.M. and N.M.; resources: A.S. and B.L.; data curation: M.Y.; writing – original draft: S.M. and A.S.; writing – review & editing; S.M., S.C., and A.S.; visualization: S.M. and A.S.; supervision: A.S.; project administration: M.Y. and A.S.; funding acquisition: A.S. and B.L.

DECLARATION OF INTERESTS

B.L. is an MMV employee.

Received: February 15, 2023
Revised: September 24, 2023
Accepted: May 17, 2024
Published: May 22, 2024

REFERENCES

1. World Health Organization (WHO) (2023). World Malaria Report.
2. Yogavel, M., Nettleship, J.E., Sharma, A., Harlos, K., Jamwal, A., Chaturvedi, R., Sharma, M., Jain, V., Chhibber-Goel, J., and Sharma, A. (2018). Structure of 6-hydroxymethyl-7,8-dihydropterin pyrophosphokinase-dihydropteroate synthase from Plasmodium vivax sheds light on drug resistance. J. Biol. Chem. *293*, 14962–14972. https://doi.org/10.1074/jbc.RA118.004558.
3. Chhibber-Goel, J., and Sharma, A. (2019). Profiles of Kelch mutations in Plasmodium falciparum across South Asia and their implications for tracking drug resistance. Int. J. Parasitol. Drugs Drug Resist. *11*, 49–58. https://doi.org/10.1016/j.ijpddr.2019.10.001.
4. Balikagala, B., Fukuda, N., Ikeda, M., Katuro, O.T., Tachibana, S.-I., Yamauchi, M., Opio, W., Emoto, S., Anywar, D.A., Kimura, E., et al. (2021). Evidence of Artemisinin-Resistant Malaria in Africa. N. Engl. J. Med. *385*, 1163–1171. https://doi.org/10.1056/nejmoa2101746.
5. Rosenthal PJ. Has artemisinin resistance emerged in Africa? Lancet Infect Dis. 2021 Aug;21(8):1056-1057. doi: 10.1016/S1473-3099(21)00168-7. Epub 2021 Apr 14. PMID: 33864802.
6. Manickam, Y., Chaturvedi, R., Babbar, P., Malhotra, N., Jain, V., and Sharma, A. (2018). Drug targeting of one or more aminoacyl-tRNA synthetase in the malaria parasite Plasmodium falciparum. Drug Discov. Today *3*, 1233–1240. https://doi.org/10.1016/j.drudis.2018.01.050.
7. Bhatt, T.K., Kapil, C., Khan, S., Jairajpuri, M.A., Sharma, V., Santoni, D., Silvestrini, F., Pizzi, E., and Sharma, A. (2009). A genomic glimpse of aminoacyl-tRNA synthetases in malaria parasite Plasmodium falciparum. BMC Genom. *10*, 644. https://doi.org/10.1186/1471-2164-10-644.
8. Gill, J., and Sharma, A. (2023). Exploration of aminoacyl-tRNA synthetases from eukaryotic parasites for drug development. J. Biol. Chem. *299*, 102860. https://doi.org/10.1016/j.jbc.2022.102860.
9. Koh, C.Y., Kim, J.E., Shibata, S., Ranade, R.M., Yu, M., Liu, J., Gillespie, J.R., Buckner, F.S., Verlinde, C.L.M.J., Fan, E., and Hol, W.G.J. (2012). Distinct states of methionyl-tRNA synthetase indicate inhibitor binding by conformational selection. Structure *20*, 1681–1691. https://doi.org/10.1016/j.str.2012.07.011.
10. Koh, C.Y., Kim, J.E., Napoli, A.J., Verlinde, C.L.M.J., Fan, E., Buckner, F.S., Van Voorhis, W.C., and Hol, W.G.J. (2013). Crystal structures of Plasmodium falciparum cytosolic tryptophanyl-tRNA synthetase and its potential as a target for structure-guided drug design. Mol. Biochem. Parasitol. *189*, 26–32. https://doi.org/10.1016/j.molbiopara.2013.04.007.
11. Koh, C.Y., Kim, J.E., Wetzel, A.B., de van der Schueren, W.J., Shibata, S., Ranade, R.M., Liu, J., Zhang, Z., Gillespie, J.R., Buckner, F.S., et al. (2014). Structures of Trypanosoma brucei Methionyl-tRNA Synthetase with Urea-Based Inhibitors Provide Guidance for Drug Design against Sleeping Sickness. PLoS Negl. Trop. Dis. *8*, e2775. https://doi.org/10.1371/journal.pntd.0002775.
12. Keller, T.L., Zocco, D., Sundrud, M.S., Hendrick, M., Edenius, M., Yum, J., Kim, Y.J., Lee, H.K., Cortese, J.F., Wirth, D.F., et al. (2012). Halofuginone and other febrifugine derivatives inhibit prolyl-tRNA synthetase. Nat. Chem. Biol. *8*, 311–317. https://doi.org/10.1038/nchembio.790.
13. Herman, J.D., Pepper, L.R., Cortese, J.F., Estiu, G., Galinsky, K., Zuzarte-Luis, V., Derbyshire, E.R., Ribacke, U., Lukens, A.K., Santos, S.A., et al. (2015). The cytoplasmic prolyl-tRNA synthetase of the malaria parasite is a dual-stage target of febrifugine and its analogs. Sci. Transl. Med. *7*, 288ra77. https://doi.org/10.1126/scitranslmed.aaa3575.
14. Jain, V., Kikuchi, H., Oshima, Y., Sharma, A., and Yogavel, M. (2014). Structural and functional analysis of the anti-malarial drug target prolyl-tRNA synthetase. J. Struct. Funct. Genomics *15*, 181–190. https://doi.org/10.1007/s10969-014-9186-x.
15. Jain, V., Yogavel, M., Oshima, Y., Kikuchi, H., Touquet, B., Hakimi, M.A., and Sharma, A. (2015). Structure of prolyl-tRNA synthetase-halofuginone complex provides basis for development of drugs against malaria and toxoplasmosis. Structure *23*, 819–829. https://doi.org/10.1016/j.str.2015.02.011.
16. Jain, V., Sharma, A., Singh, G., Yogavel, M., and Sharma, A. (2017). Structure-Based Targeting of Orthologous Pathogen Proteins Accelerates Antiparasitic Drug Discovery. ACS Infect. Dis. *3*, 281–292. https://doi.org/10.1021/acsinfecdis.6b00181.
17. Jain, V., Yogavel, M., Kikuchi, H., Oshima, Y., Hariguchi, N., Matsumoto, M., Goel, P., Touquet, B., Jumani, R.S., Tacchini-Cottier, F., et al. (2017). Targeting Prolyl-tRNA Synthetase to Accelerate Drug Discovery against Malaria, Leishmaniasis, Toxoplasmosis, Cryptosporidiosis, and Coccidiosis. Structure *25*, 1495–1505.e6. https://doi.org/10.1016/j.str.2017.07.015.
18. Mishra, S., Malhotra, N., Kumari, S., Sato, M., Kikuchi, H., Yogavel, M., and Sharma, A. (2019). Conformational heterogeneity in apo and drug-bound structures of Toxoplasma gondii prolyl-tRNA synthetase. Acta Crystallogr. F Struct. Biol. Commun. *75*, 714–724. https://doi.org/10.1107/S2053230X19014808.
19. Vinayak, S., Jumani, R.S., Miller, P., Hasan, M.M., McLeod, B.I., Tandel, J., Stebbins, E.E., Teixeira, J.E., Borrel, J., Gonse, A., et al. (2020). Bicyclic azetidines kill the diarrheal pathogen Cryptosporidium in mice by inhibiting parasite phenylalanyl-tRNA synthetase. Sci. Transl. Med. *12*, eaba8412. https://doi.org/10.1126/scitranslmed.aba8412.
20. Babbar, P., Sato, M., Manickam, Y., Mishra, S., Harlos, K., Gupta, S., Parvez, S., Kikuchi, H., and Sharma, A. (2021). Inhibition of Plasmodium falciparum Lysyl-tRNA synthetase via a piperidine-ring scaffold inspired Cladosporin analogues. Chembiochem *22*, 2468–2477.
21. Kato, N., Comer, E., Sakata-Kato, T., Sharma, A., Sharma, M., Maetani, M., Bastien, J., Brancucci, N.M., Bittker, J.A., Corey, V., et al. (2016). Diversity-oriented synthesis yields novel multistage antimalarial inhibitors. Nature *538*, 344–349. https://doi.org/10.1038/nature19804.
22. Hewitt, S.N., Dranow, D.M., Horst, B.G., Abendroth, J.A., Forte, B., Hallyburton, I., Jansen, C., Baragaña, B., Choi, R., Rivas, K.L., et al. (2017). Biochemical and structural characterization of selective allosteric inhibitors of the Plasmodium falciparum drug target, prolyl-tRNA-synthetase. ACS Infect. Dis. *3*, 34–44. https://doi.org/10.1021/acsinfecdis.6b00078.

23. Sharma, M., Malhotra, N., Yogavel, M., Harlos, K., Melillo, B., Comer, E., Gonse, A., Parvez, S., Mitasev, B., Fang, F.G., et al. (2021). Structural basis of malaria parasite phenylalanine tRNA-synthetase inhibition by bicyclic azetidines. Nat. Commun. *12*, 343. https://doi.org/10.1038/s41467-020-20478-5.
24. Nachiappan, M., Jain, V., Sharma, A., Yogavel, M., and Jeyakanthan, J. (2018). Structural and functional analysis of Glutaminyl-tRNA synthetase (TtGlnRS) from Thermus thermophilus HB8 and its complexes. Int. J. Biol. Macromol. *120*, 1379–1386. https://doi.org/10.1016/j.ijbiomac.2018.09.115.
25. Baragaña, B., Forte, B., Choi, R., Nakazawa Hewitt, S., Bueren-Calabuig, J.A., Pisco, J.P., Peet, C., Dranow, D.M., Robinson, D.A., Jansen, C., et al. (2019). Lysyl-tRNA synthetase as a drug target in malaria and cryptosporidiosis. Proc. Natl. Acad. Sci. USA *116*, 7015–7020. https://doi.org/10.1073/pnas.1814685116.
26. Radke, J.B., Melillo, B., Mittal, P., Sharma, M., Sharma, A., Fu, Y., Uddin, T., Gonse, A., Comer, E., Schreiber, S.L., et al. (2022). Bicyclic azetidines target acute and chronic stages of Toxoplasma gondii by inhibiting parasite phenylalanyl t-RNA synthetase. Nat. Commun. *13*, 459. https://doi.org/10.1038/s41467-022-28108-y.
27. Tye, M.A., Payne, N.C., Johansson, C., Singh, K., Santos, S.A., Fagbami, L., Pant, A., Sylvester, K., Luth, M.R., Marques, S., et al. (2022). Elucidating the path to Plasmodium prolyl-tRNA synthetase inhibitors that overcome halofuginone resistance. Nat. Commun. *13*, 4976. https://doi.org/10.1038/s41467-022-32630-4.
28. Zhou, H., Sun, L., Yang, X.L., and Schimmel, P. (2013). ATP-directed capture of bioactive herbal-based medicine on human tRNA synthetase. Nature *494*, 121–124. https://doi.org/10.1038/nature11774.
29. Manickam, Y., Malhotra, N., Mishra, S., Babbar, P., Dusane, A., Laleu, B., Bellini, V., Hakimi, M.A., Bougdour, A., and Sharma, A. (2022). Double drugging of prolyl-TRNA synthetase provides a new paradigm for anti-infective drug development. PLoS Pathog. *18*, e1010363. https://doi.org/10.1371/journal.ppat.1010363.
30. Shibata, A., Kuno, M., Adachi, R., Sato, Y., Hattori, H., Matsuda, A., Okuzono, Y., Igaki, K., Tominari, Y., Takagi, T., et al. (2017). Discovery and pharmacological characterization of a new class of prolyl-tRNA synthetase inhibitor for anti-fibrosis therapy. PLoS One *12*, e0186587. https://doi.org/10.1371/journal.pone.0186587.
31. Gill, J., and Sharma, A. (2022). Prospects of halofuginone as an antiprotozoal drug scaffold. Drug Discov. Today *27*, 2586–2592. https://doi.org/10.1016/j.drudis.2022.05.020.
32. Adachi, R., Okada, K., Skene, R., Ogawa, K., Miwa, M., Tsuchinaga, K., Ohkubo, S., Henta, T., and Kawamoto, T. (2017). Discovery of a novel prolyl-tRNA synthetase inhibitor and elucidation of its binding mode to the ATP site in complex with L-proline. Biochem. Biophys. Res. Commun. *488*, 393–399. https://doi.org/10.1016/j.bbrc.2017.05.064.
33. Okaniwa, M., Shibata, A., Ochida, A., Akao, Y., White, K.L., Shackleford, D.M., Duffy, S., Lucantoni, L., Dey, S., Striepen, J., et al. (2021). Repositioning and Characterization of 1-(Pyridin-4-yl)pyrrolidin-2-one Derivatives as Plasmodium Cytoplasmic Prolyl-tRNA Synthetase Inhibitors. ACS Infect. Dis. *7*, 1680–1689. https://doi.org/10.1021/acsinfecdis.1c00020.
34. Yogavel, M., Bougdour, A., Mishra, S., Malhotra, N., Chhibber-Goel, J., Bellini, V., Harlos, K., Laleu, B., Hakimi, M.A., and Sharma, A. (2023). Targeting prolyl-tRNA synthetase via a series of ATP-mimetics to accelerate drug discovery against toxoplasmosis. PLoS Pathog. *19*, e1011124. https://doi.org/10.1371/journal.ppat.1011124.
35. Zhou, H., Sun, L., Yang, X.L., and Schimmel, P. (2013). ATP-directed capture of bioactive herbal-based medicine on human tRNA synthetase. Nature *494*, 121–124. https://doi.org/10.1038/nature11774.
36. Lee, E.Y., Kim, S., and Kim, M.H. (2018). Aminoacyl-tRNA synthetases, therapeutic targets for infectious diseases. Biochem. Pharmacol. *154*, 424–434. https://doi.org/10.1016/j.bcp.2018.06.009.
37. Kwon, N.H., Fox, P.L., and Kim, S. (2019). Aminoacyl-tRNA synthetases as therapeutic targets. Nat. Rev. Drug Discov. *18*, 629–650. https://doi.org/10.1038/s41573-019-0026-3.
38. Francklyn, C.S., and Mullen, P. (2019). Progress and challenges in aminoacyl-tRNA synthetase-based therapeutics. J. Biol. Chem. *294*, 5365–5385. https://doi.org/10.1074/jbc.REV118.002956.
39. Kelly, P., Hadi-Nezhad, F., Liu, D.Y., Lawrence, T.J., Linington, R.G., Ibba, M., and Ardell, D.H. (2020). Targeting tRNA-synthetase interactions towards novel therapeutic discovery against eukaryotic pathogens. PLoS Negl. Trop. Dis. *14*, e0007983. https://doi.org/10.1371/journal.pntd.0007983.
40. Khan, S., Sharma, A., Belrhali, H., Yogavel, M., and Sharma, A. (2014). Structural basis of malaria parasite lysyl-tRNA synthetase inhibition by cladosporin. J. Struct. Funct. Genomics *15*, 63–71. https://doi.org/10.1007/s10969-014-9182-1.
41. Jain, V., Yogavel, M., Oshima, Y., Kikuchi, H., Touquet, B., Hakimi, M.A., and Sharma, A. (2015). Structure of prolyl-tRNA synthetase-halofuginone complex provides basis for development of drugs against malaria and toxoplasmosis. Structure *23*, 819–829. https://doi.org/10.1016/j.str.2015.02.011.
42. Arita, T., Morimoto, M., Yamamoto, Y., Miyashita, H., Kitazawa, S., Hirayama, T., Sakamoto, S., Miyamoto, K., Adachi, R., Iwatani, M., and Hara, T. (2017). Prolyl-tRNA synthetase inhibition promotes cell death in SK-MEL-2 cells through GCN2-ATF4 pathway activation. Biochem. Biophys. Res. Commun. *488*, 648–654. https://doi.org/10.1016/j.bbrc.2017.01.045.
43. Baykov, A.A., Evtushenko, O.A., and Avaeva, S.M. (1988). A malachite green procedure for orthophosphate determination and its use in alkaline phosphatase-based enzyme immunoassay. Anal. Biochem. *171*, 266–270. https://doi.org/10.1016/0003-2697(88)90484-8.
44. Jarmoskaite, I., Alsadhan, I., Vaidyanathan, P.P., and Herschlag, D. (2020). How to measure and evaluate binding affinities. Elife *9*, 572644–e57334. https://doi.org/10.7554/ELIFE.57264.
45. Trager, W., and Jensen, J.B. (1976). Human malaria parasites in continuous culture. Science *193*, 673–675. https://doi.org/10.1126/science.781840.
46. Tonkin, C.J., Van Dooren, G.G., Spurck, T.P., Struck, N.S., Good, R.T., Handman, E., Cowman, A.F., and McFadden, G.I. (2004). Localization of organellar proteins in Plasmodium falciparum using a novel set of transfection vectors and a new immunofluorescence fixation method. Mol. Biochem. Parasitol. *137*, 13–21. https://doi.org/10.1016/j.molbiopara.2004.05.009.
47. Smilkstein, M., Sriwilaijaroen, N., Kelly, J.X., Wilairat, P., and Riscoe, M. (2004). Simple and Inexpensive Fluorescence-Based Technique for High-Throughput Antimalarial Drug Screening. Antimicrob. Agents Chemother. *48*, 1803–1806. https://doi.org/10.1128/AAC.48.5.1803-1806.2004.
48. Winter, G., Waterman, D.G., Parkhurst, J.M., Brewster, A.S., Gildea, R.J., Gerstel, M., Fuentes-Montero, L., Vollmar, M., Michels-Clark, T., Young, I.D., et al. (2018). DIALS : implementation and evaluation of a new integration package. Acta Crystallogr. Sect. D Struct. Biol. *74*, 85–97. https://doi.org/10.1107/s2059798317017235.
49. McCoy, A.J., Grosse-Kunstleve, R.W., Adams, P.D., Winn, M.D., Storoni, L.C., and Read, R.J. (2007). Phaser crystallographic software. J. Appl. Crystallogr. *40*, 658–674. https://doi.org/10.1107/S0021889807021206.
50. Adams, P.D., Afonine, P.V., Bunkóczi, G., Chen, V.B., Davis, I.W., Echols, N., Headd, J.J., Hung, L.W., Kapral, G.J., Grosse-Kunstleve, R.W., et al. (2010). PHENIX: A comprehensive Python-based system for macromolecular structure solution. Acta Crystallogr. Sect. D Biol. Crystallogr. *66*, 213–221. https://doi.org/10.1107/S0907444909052925.
51. Emsley, P., and Cowtan, K. (2004). Coot: Model-building tools for molecular graphics. Acta Crystallogr. D Biol. Crystallogr. *60*, 2126–2132. https://doi.org/10.1107/S0907444904019158.
52. Williams, C.J., Headd, J.J., Moriarty, N.W., Prisant, M.G., Videau, L.L., Deis, L.N., Verma, V., Keedy, D.A., Hintze, B.J., Chen, V.B., et al. (2018). MolProbity: More and better reference data for improved all-atom structure validation. Protein Sci. *27*, 293–315. https://doi.org/10.1002/pro.3330.
53. Adasme, M.F., Linnemann, K.L., Bolz, S.N., Kaiser, F., Salentin, S., Haupt, V.J., and Schroeder, M. (2021). PLIP 2021: expanding the scope of the protein-ligand interaction profiler to DNA and RNA. Nucleic Acids Res *49* (W1), W530–W534. https://doi.org/10.1093/nar/gkab294.
54. Pettersen, E.F., Goddard, T.D., Huang, C.C., Couch, G.S., Greenblatt, D.M., Meng, E.C., and Ferrin, T.E. (2004). UCSF Chimera–a visualization system for exploratory research and analysis. J. Comput. Chem. *25*, 1605–1612. https://doi.org/10.1002/jcc.20084.

STAR★METHODS

KEY RESOURCES TABLE

REAGENT or RESOURCE	SOURCE	IDENTIFIER
Chemicals, peptides, and recombinant proteins		
IPTG	G-Biosciences	367-93-1
Tris Base, Molecular Biology Grade	Sigma-Aldrich	77-86-1
Hydrochloric Acid	Sigma-Aldrich	7647-01-0
HEPES	Sigma-Aldrich	7365-45-9
Sodium Hydroxide Pellets	Sigma-Aldrich	1310-73-2
Sodium Chloride	Sigma-Aldrich	7647-14-5
2-Mercaptoethanol	Sigma-Aldrich	60-24-2
1,4-Dithiothreitol	Sigma-Aldrich	3483-12-3
EDTA disodium salt dihydrate	Sigma-Aldrich	6381-92-6
Glycerol	HiMedia	GRM1027
Imidazole	HiMedia	GRM559
Maltose Monohydrate	Sigma-Aldrich	6363-53-7
Potassium Chloride	Sigma-Aldrich	7447-40-7
Magnesium Chloride	Sigma-Aldrich	7786-30-3
Tween 20	Sigma-Aldrich	9005-64-5
L-proline	Sigma-Aldrich	147-85-3
Na-ATP	Sigma-Aldrich	34369-07-8
Hypoxanthine	Sigma-Aldrich	68-94-0
Gentamicin	Sigma-Aldrich	1405-41-0
Saponin	Sigma-Aldrich	8047-15-2
Deposited data		
PDB ID – 7F96; *Plasmodium falciparum* Prolyl-tRNA Synthetase (PfPRS) in Complex with L-proline and compound L95	This Paper	https://doi.org/10.2210/pdb7F96/pdb
PDB ID – 7F97; *Plasmodium falciparum* Prolyl-tRNA Synthetase (PfPRS) in Complex with L-proline and compound L97.	This Paper	https://doi.org/10.2210/pdb7F97/pdb
Experimental models: Cell lines		
Plasmodium falciparum 3D7 Strain	BEI Resources	MRA-102
Software and algorithms		
Protein Thermal Shift Software	Applied Biosystems by Thermofisher	https://www.fishersci.fi/shop/products/protein-thermal-shift-software-v1-4/15440340
GraphPad Prism Version 6.0.0 for Windows	GraphPad Software, San Diego, California, USA.	www.graphpad.com
NanoTemper Monolith Instrument (NT.115) Control and Analysis Software Package	NanoTemper	https://nanotempertech.com/microscale-thermophoresis/
DIALS, CCP4.	Winter et al., 2018[48]	https://www.ccp4.ac.uk/download/#os=mac
Phenix	Adams et al., 2010[50]	https://phenix-online.org/download/
Phaser	McCoy et al., 2007[49]	Within Phenix
Coot	Emsley et al., 2004[51]	https://scottlab.ucsc.edu/xtal/coot/
Chimera	Pettersen et al., 2004[54]	https://www.cgl.ucsf.edu/chimera/download.html

(*Continued on next page*)

Continued

REAGENT or RESOURCE	SOURCE	IDENTIFIER
MolProbity	Williams et al., 2018[52]	Within Phenix Refine
PLIP	Adasme et al., 2021[53]	https://plip-tool.biotec.tu-dresden.de/plip-web/plip/index

RESOURCE AVAILABILITY

Lead contact

Further information and request regarding the resources should be directed to the lead contact, Siddhartha Mishra (siddhartha96123@gmail.com).

Materials availability

This study did not generate any new unique reagents.

Data and code availability

- The PDB IDs 7F96 and 7F97 have been deposited at the Protein Data Bank and are now publicly available. The link for the same is available in the key resources table.
- No new original code was generated within this study to be made publicly available.
- Any additional information required to re-analyze the data reported in this paper is available from the lead contact upon request.

EXPERIMENTAL MODEL AND STUDY PARTICIPANT DETAILS

This study uses the 3D7 *Plasmodium falciparum* strain from BEI resources with identifier MRA-102 for the *in vitro* experiments. No *in vivo* or human studies have been performed as part of this study.

METHOD DETAILS

Protein purification

P. falciparum PRS and *H. sapiens* PRS were purified following previously published methods.[17] Briefly, protein expression was induced by adding 0.6 mM isopropyl b-D-thiogalactopyranoside (IPTG) to cells grown at 37°C for 4 h and 18 h post-induction at 18°C. Cells were harvested by centrifugation at 4500 *g* for 20 min. The bacterial pellet was suspended in a buffer containing 50 mM Tris–HCl pH 8.0, 200 mM NaCl, 3 mM βME, 15% v/v glycerol, 0.1 mg mL^{-1} lysozyme and EDTA-free protease inhibitor cocktail (Roche). Cells were lysed by sonication and cleared by centrifugation at 13000 *g* for 45 min. The cleared supernatant with MBP and His_6 tagged proteins was applied to amylose beads (NEB) or NiNTA beads (GE). Protein was eluted with buffer 50 mM Tris–HCl pH 8.0, 200 mM NaCl, 10 mM β-mercaptoethanol (βME), and 25 mM maltose or increasing concentration gradient of imidazole from 10 mM to 1 M, respectively. The eluted protein fractions were dialyzed against 30 mM HEPES pH 7.5, 20 mM NaCl, 1 mM DTT, and 0.5 mM EDTA (buffer A). The protein was further purified by heparin chromatography (GE Healthcare) using NaCl gradients with buffer B containing 30 mM HEPES pH 7.5, 500 mM NaCl, 1 mM DTT, and 0.5 mM EDTA. A protein peak was found at 40% buffer B. The tags (MBP and His tag) were removed by incubating with TEV protease at 20°C overnight. Cleaved *Pf*PRS and *Hs*PRS proteins were concentrated using a 10 kDa cut-off Centricon centrifugal device (Millipore) and purified by gel filtration chromatography on Superdex 200 column 16/60 GL (GE Healthcare) equilibrated with 20 mM HEPES pH 7.5, 200 mM NaCl and 2 mM DTT. Bovine serum albumin (66 kDa, Sigma) was used as a standard for molecular mass estimation. SDS-PAGE checked eluted fractions, and pure ones were pooled, concentrated and stored at −80°C.

Thermal stability assays

Fluorescence-based TSAs were performed to assess the binding potencies of the five novel ATP mimetics for *Pf*PRS and *Hs*PRS in the presence or absence of substrates (L-pro and ATP). Purified PRS enzymes with their substrates and inhibitors were heated from 25°C to 99 °C at 1 °C min^{-1}. A quantitative real-time PCR system monitored fluorescence signals of the SYPRO orange dye (Life Technologies). The 'Enzyme: Compound' ratios maintained were 1:50 for the *Pf* (1:50 μM) enzyme and 1:100 for the *Hs* (1:100 μM) enzyme. The substrates were at saturating concentrations of 2 mM. The high ratio with the human enzyme was utilized to capture any sub-populations Tm for any specific condition. The displayed melt temperature averages three measurements, and data were analyzed using Protein Thermal shift software (v1.3, Thermofisher). The controls used included the inhibitors and substrates alone in assay buffers, and no PRS enzyme and flat lines were observed for these fluorescence readings across the temperatures. HFG was used as an additional positive reference for the assay. Analysis of specific mixed species of 'enzyme-ligand' complexes was performed. The 'Rule of Elimination' was utilized to analyze unique individual melt temperatures when multiple products/complexes are likely to be formed in the reaction well. This was not done based on the peak height (the ratio of the areas under the different peaks might shed light on the fraction of sub-populations). For instance, in a situation where the control/previous

experiment shows T1 is the Tm for some condition C1 and for a condition C2 two peaks manifest at temperatures T1 and T2. In this case, while analyzing the Tm for C2, we followed T2 and not T1.

Enzyme inhibition assays

All enzymatic assays were done as per previously established methods.[16,43] Standard aminoacylation buffer reagents include 30 mM HEPES buffer (pH 7.5), 140 mM NaCl, 30 mM KCl, 40 mM $MgCl_2$, 1 mM DTT, 25 μM ATP, 25 μM L-pro and 400 nM recombinant PRSs. For the inhibition assays in particular – the compounds were incubated with the novel ATP mimetics at 50 μM to 0.05 nM in 100 μL and incubated for about 100 min at 37°C. Guidelines for deciding on the concentration and incubation time for computing half-maximal values have been explored by Jarmoskaite et al..[44] This allowed us to use the best combination that provided for plateauing of the readout and the colorimetric visual saturation of the aminoacyl-adenylate forming reaction. Figure S4 shows the rationale for using this concentration and incubation time regime for the PRSs.

Consequently, normalized percentage inhibition of aminoacylation activity was plotted as a function of the log of compound concentration. Data were fit to a sigmoidal curve for nonlinear regression analysis using GraphPad Prism version 6.0.0 for Windows, GraphPad Software, San Diego, California USA, (www.graphpad.com). Selectivity Indices were computed by arithmetically dividing the host parameter by the parasitic parameter, i.e., the IC_{50} of the human enzyme divided by that of the plasmodium enzyme.

P. falciparum culture and assays

Plasmodium falciparum 3D7 strain was cultured in O^+ erythrocytes in RPMI 1640 (Invitrogen, USA) supplemented with 0.1 mM hypoxanthine (Invitrogen, USA), 25 mg mL^{-1} gentamicin (Invitrogen, USA) and 0.5% AlbuMax-I (Invitrogen, USA), according to standard methods.[45] Parasites were sorbitol-treated in ring stages to maintain a synchronized culture.[46] *Plasmodium falciparum* was cultured in 96-well plates and synchronized at ring stages. All compounds were prepared as stocks at 20 mM in 100% DMSO. At ~1% parasitaemia and 4% haematocrit, inhibitor concentrations ranging from 0.001 nM to 10 μM were incubated for 48 h with the parasites. Growth was assayed by SYBR green-I (Molecular probes) DNA staining assays as described earlier.[47] Briefly, 100 μL SYBR green dye in 2× concentration in lysis buffer supplemented with 0.1% saponin was added to each well. After 45 min incubation at 37°C, fluorescence was estimated using a multi-well plate reader (Victor 3, PerkinElmer) with excitation and emission wavelength bands centered at 485 and 530 nm, respectively. CQ and Dihydroartemisinin (DHA) were taken as positive controls, and all experiments were in triplicates. The EC50 values were obtained by plotting fluorescence values expressed in terms of the percentage of parasite growth at each inhibitor concentration. Analyses were done using nonlinear regression analysis with GraphPad Prism 6 software. All data are shown for two biological replicates, each with three technical replicates as means with standard errors. These data with previously published ARPE19 and MDA231 cell lines toxicity screen data of CC50 were used to compute cellular and enzymatic selectivity indices (See Tables 2 and S2).

Binding affinity (K_d) determination via Microscale Thermophoresis

A NanoTemper Monolith Instrument (NT.115) was used for measuring thermophoresis. Purified *Pf*PRS *and Hs*PRS were labeled with the Red-NHS 2nd generation lysine-labelling dye. All compounds including HFG, L95, L96, L97, L35 and L36 were titrated (0.0005 nM–5 μM) against 100 nM of labeled *Pf*PRS and *Hs*PRS in 20 mM HEPES pH 7.5, 200 mM NaCl, 2 mM DTT, 10 mM $MgCl_2$ and 0.05% Tween 20 buffer in addition to 100 nM L-proline and 1μM ATP in two independent replicate experiments ($n = 2$). The samples were incubated at room temperature for 30 min and were loaded into MST hydrophilic-treated premium glass capillaries. MST was performed using 100% excitation and 40% MST power at 30°C. All K_d values were computed by guidance of validation by acceptable statistical range parameters (RA $\geq$ 6; Signal to Noise Ratio (STN) $\geq$ 2; Standard error of regression (SER) $\leq$ 3) and analyzed using Nano Temper software (https://support.nanotempertech.com/hc/en-us/articles/18006927752209-Monolith-NT-115-User-Manual-). $K_{d\text{-mean}}$ values were calculated for each and have been displayed in bold in Figure 3. HFG was used as a positive control to check if MST is a reliable methodology (Figure S5). The drastically reduced K_d value of HFG with both natural ligands compared to that with the apo *Hs*PRS aligned with previously computed values (Figures 3 and S5).[41]

Crystallization

Highly purified *Pf*PRS enzyme at 12–15 mg mL^{-1} was used for crystallization via the hanging-drop vapour-diffusion method at 20°C using commercially available crystallization screens (Hampton Research and Molecular Dimensions). Initial screening was performed in 96-well plates using a nanodrop dispensing Mosquito robot (TTP Labtech). Three different drop ratios of purified protein and reservoir (i.e., 1:1, 2:1 and 1:2 drop ratios) were used for the crystallization trials. Each drop was equilibrated against 100 mL of the corresponding reservoir solution. Before crystallization, 1 to 3 mM compounds and 2 mM L-Pro were added to the PRS enzyme, and the mixtures were incubated at 4°C for 10 min. The diffraction quality crystals were obtained at 20°C by the hanging-drop vapour-diffusion method. The crystallization conditions and relevant statistics for each enzyme-inhibitor complex are listed in Table 4.

Structure determination and analyses

The X-ray diffraction preliminary datasets were collected on beamline I03 at Diamond Light Source, United Kingdom. Final data collection was performed in SOLEIL PROXIMA 1. The auto-processing pipelines processed the data using DIALS[48] and XDS for integration. The initial models were determined by the molecular replacement method using Phaser[49] and PDB 4YDQ (*Pf*PRS-HFG-AMPPMP)[41] as the template.

The structures were refined by iterative cycles with Phenix[50] and model building with COOT.[51] Map interpretations and model building were based on electron densities in Fourier ($F_o - F_c$) and $2F_o - F_c$ maps. Model building was guided by manual inspection of the model and R_{free} in all stages. The substrate/inhibitor and water molecules were added based on the difference Fourier maps ($F_o - F_c$). The occupancies of the ligand molecules were refined, and highly disordered loop regions were not included in the final model. The stereochemical quality of the models was assessed and corrected using MolProbity.[52] The summary of the refined parameters is given in Table 4. All interactions within the protein assemblies and with the ligands were assessed utilizing the PLIP server.[53] The figures were prepared using Chimera.[54]

QUANTIFICATION AND STATISTICAL ANALYSIS

Statistical analyses for all the assays have been performed utilizing rational approaches of data interpretation. A minimum of two independent replicates with technical triplicates were utilized for computation with means as standard errors. Correlation coefficients of the IC_{50} and EC_{50} assays were computed with the aid of GraphPad software. Assay fidelity was trusted upon with a threshold of 0.7 for the R^2 values. MST and TSA data were analyzed using arithmetic mean rationales. Individual datasets of the MST and TSA experiments were selected only when individual statistics were in acceptable ranges as mentioned in the method details of each.